Extreme Mechanics Letters 79 (2025) 102379

Contents lists available at ScienceDirect

Extreme Mechanics Letters

journal homepage: www.elsevier.com/locate/eml

Band gap analysis and prediction for phononic metamaterials with different spiral shapes based on transfer learning

Majid Kheybari, Hongyi Xu *

School of Mechanical, Aerospace, and Manufacturing Engineering, University of Connecticut, 191 Auditorium Rd, Storrs, 06269, CT, USA

ARTICLE INFO

Keywords:
Metamaterials
Phononic band gap
Band gap prediction
Archimedean spiral
Polygon-based spirals
Neural network
Transfer learning

ABSTRACT

This study presents a comprehensive computational investigation of band gap characteristics in spiral-based phononic metamaterials, including Archimedean, Octagon, Hexagon, and Square spiral configurations. It offers a quantitative understanding of the similarities in Bloch wave properties across these spiral types and demonstrates the feasibility of using data from known spiral patterns to facilitate the property prediction of new types. Based on the spiral datasets that vary in the number of turns, cutting width, and inner radius, we observed strong correlations in band gap counts among patterns (e.g., Rotated Octagon and Octagon, Archimedean and Rotated Octagon), indicating similar behaviors in band gap occurrence across different geometries. It was also found that the rotation of geometric shapes had a minor impact on band gap counts. However, we observed that the distribution of band gap width varies significantly across different types of spirals, with weak correlations. Furthermore, we demonstrate that transfer learning (TL) enhances prediction accuracy for new spiral types compared to traditional neural network approaches. TL model demonstrated superior performance, effectively capturing complex band gap details and improving overall prediction accuracy, without requiring extensive training data.

1. Introduction

In this computational investigation, we analyze the dynamics of different spiral-based phononic metamaterials and apply transfer learning to predict their band gaps with minimal data, providing an efficient framework for designing novel phononic structures. Extensive research has been conducted on locally resonant elastic/acoustic metamaterials [1,2] and phononic crystals [3,4] due to their intriguing dynamic characteristics, particularly the presence of band gaps where elastic or acoustic waves cannot propagate. Phononic crystals typically consist of periodic arrangements of unit cells [5], whereas locally resonant metamaterials rely on local resonance rather than periodicity to achieve their unique properties. When periodicity is present, Bloch's theorem can be applied to calculate the band structure [6]. In locally resonant elastic/acoustic metamaterials, hybridization between dispersion and local resonance can generate local resonance band gaps [7]. In contrast, phononic crystals produce Bragg scattering band gaps due to periodicity and impedance mismatches between unit cells [8].

These band gaps enable a wide range of applications, including wave-guiding [9,10], filtering [11,12], wave localization [13,14], biomedical devices [15,16], and sound insulation [17,18]. Additionally, locally resonant structures can exhibit unusual dynamic properties, such as negative effective parameters, including Poisson's ratio [19,20], mass density [21,22], and stiffness [23,24]. These properties facilitate novel applications in areas such as cloaking [25,26] and focusing [27,28].

The unique properties of metamaterials arise not from the intrinsic characteristics of the constituent materials, but from their precisely engineered shape, unit cell type, geometry, size, orientation, and arrangement. These factors can impact not only the functionality, but also the feasibility of mass production, making the selection process crucial in both research and industrial applications [29–33]. For instance, the study of different unit cells with various symmetries and scatterers of shapes such as hexagons, circles, squares, and triangles, along with their orientations and sizes, shows that for triangular, square, and honeycomb lattices, the most significant absolute phononic band gap (PBG) can be achieved by using rods with shapes that match the coordination polygons of the lattice points: hexagonal rods in triangular lattices, square rods in square lattices, and triangular rods in honeycomb lattices. In another study, a spider-web metamaterial structure was proposed, in which circular elements were embedded

* Corresponding author.
E-mail address: hongyi.3.xu@uconn.edu (H. Xu).

https://doi.org/10.1016/j.eml.2025.102379
Received 4 November 2024; Received in revised form 31 May 2025; Accepted 6 July 2025
Available online 22 July 2025

within a supporting frame to induce a phononic band gap; the effects of material parameters were systematically investigated by employing either identical or distinct material properties for the spider-web structure and the frame [34]. Moreover, the band gap can be altered by changing the orientation and size of the scatterers [35]. By adjusting geometrical parameters, such as the pillar height in a square lattice of cylindrical pillars on a substrate, it is possible to create multiple band gaps. As the height of the pillars increases, the frequency bands shift to lower frequencies, and new band gaps appear [36]. Additionally, altering the height of the stubs within the phononic plate can influence the formation of the band gap. Increasing the height of the stubs leads to the formation of a Dirac cone, breaking the inversion symmetry, and resulting in a complete band gap [37]. Furthermore, studies of three-dimensional helical metamaterial tapered rods with different radii show that increasing the initial radius while reducing both the residual radius and the tapered helical region can enhance the local resonance effect, effectively broadening the band gap [38].

Various geometries have been explored to influence the band gap of phononic metamaterials, with spiral resonators being one that has attracted significant attention from researchers [39]. Spiral patterns are significant not only in nature but also in science due to their unique structural and functional properties. In nature, spiral patterns are prevalent in various forms, such as the arrangement of sunflower seeds, the shells of mollusks, and the growth of galaxies [40,41]. Beyond their natural occurrences, spirals play a crucial role in scientific and engineering disciplines. In materials science, spiral geometries are utilized in the design of metamaterials to achieve desired resonant behaviors and manipulate wave propagation. While Archimedes first studied spiral curves in the third century BC, researchers today continue to explore their complexity and applications [41–44].

Periodic spiral resonators with various patterns have been investigated numerically and experimentally in phononic crystals for low-frequency band gaps. For instance, a phononic crystal plate with an Archimedean spiral resonator having a fixed steel cylinder in its center has been proposed to observe a band gap in the lower frequency range (42–150 Hz). When the frequency of incident elastic waves approaches the natural frequencies of the internal spring-mass system, local resonance is triggered, generating a reactive force that opposes the harmonic wave excitation on the plate. This interaction reduces or cancels out the plate's vibration, preventing elastic waves near the natural resonance frequencies from propagating through the phononic crystal, leading to the formation of low-frequency band gaps. It has been shown that the edges of the band gap can be modulated by varying the geometrical parameters such as the thickness of the plate, the angle of the spiral beam, the width of the spiral beam, the radius of the cylinder, and the height of the cylinder [45]. In another study, multiple Archimedean spirals within a square honeycomb structure were studied for low-frequency band gaps. This model created multiple complete band gaps below 500 Hz. Results have shown that by adjusting the spiral arrangement, spiral geometry, and material parameters, the position and width of the frequency band gaps can be optimized. This model has potential applications in noise and vibration control [46]. Additionally, by modulating spiral parameters such as chirality, rotation angle, number of turns, and spiral thickness, topological properties can be achieved, specifically Berry curvature and valley Chern number [47]. Other Archimedean spiral unit cells have been reported for various applications, including wave localization at extremely low frequencies [48], designing metasurfaces as haptic interfaces [49], low-frequency vibration and noise reduction [45], reprogramming nonlinear metamaterials on-the-fly with no moving parts [50], isolating low-frequency vibrations (15–45 Hz) to protect electronic devices and precision instruments on ships [51], and realizing a topological transition [52].

There are other studies that have investigated different spiral patterns, such as square spirals, as local resonant phononic crystals to achieve low-frequency band gaps. These include local resonant phononic crystals with four square spiral elastic beams surrounding a square inclusion [53], square spirals with four circles inside [54], square spirals connecting a square frame to an internal base with a cylinder mounted on the base [55], double square spirals surrounding a square inclusion [56], and three square spiral rings covered by a square frame with a square scatter in the middle of the unit cell [57]. These studies have examined how various parameters, such as spiral beam thickness, side length of the spiral, length of the elastic beam base, number of turns, radius of the inner arc, thickness of the central mass, and the number of parasitic beam segments, affect the band gap. The proposed models have potential applications in vibration energy harvesting devices, vibration filtering systems, vibration attenuation and sound insulation.

Several other spiral-based phononic crystals and elastic/acoustic metamaterials have been reported in the literature. For instance, a spiral rod–mass unit cell has been proposed, demonstrating a large band gap at low frequencies. This structure exhibits static effective stiffness, confirming its suitability for practical applications [58]. Fibonacci-array-inspired metamaterials, composed of metamaterial bricks with unique physical mechanisms, have also been developed. These structures demonstrate low-frequency sound absorption capabilities, with potential applications in customizable absorption, scalability, and ease of manufacturing [59]. Additionally, a spiral shaft-based metamaterial has been introduced to manipulate vibration transmission characteristics, enabling applications in unidirectional vibration isolation bushings across a wide frequency range [60].

Several methods such as plane-wave expansion (PWE) [61–63], finite-difference time-domain (FDTD) [64–66], lumped mass [67–69], wavelet-based [70–72], multiple scattering theory (MST) [73–75], transfer matrix [76–78], energy [79–81], and reduced-order models [82–84] have been employed to predict phonon dispersion curves. As phononic metamaterial structures are highly complex and present considerable challenges in various domains, researchers have extensively used finite element methods (FEM) [45–57,85–94] to address the difficulties encountered in these applications.

Additionally, topology optimization is widely used to enhance the design of phononic and photonic crystals, as well as metamaterials [95]. Topology optimization, based on the FEM and genetic algorithms, enables the design of two-dimensional phononic crystals to maximize the relative width of their band gaps [96]. Parameter optimization techniques have also been applied to web-inspired phononic crystals to achieve maximum band gap widths [97]. Furthermore, artificial intelligence (AI)-based approaches for predicting dispersion curves in phononic crystals are often integrated with optimization methods to enhance design efficiency [98] or to optimize the design of metamaterials in order to maximize stiffness and Poisson's ratio, while minimizing the thermal expansion coefficient in all directions [99]. Moreover, in recent years, machine learning has emerged as a promising artificial intelligence technique to address various challenges in phononic metamaterials [100–104]. This approach involves algorithms that automatically analyze data, identify underlying patterns, and use these patterns to predict unknown data [105,106].

Machine learning (ML) methods, such as neural networks, can represent these learned patterns through continuous and differentiable functions, enabling rapid and precise problem-solving. This makes machine learning a valuable tool in developing efficient and accurate solutions for phononic metamaterials [107–111]. For instance, the properties of phononic crystals can be predicted using various machine learning algorithms, including logistic/linear regression, random forests, and artificial neural networks [112]. Additionally, a data-driven approach for designing phononic crystals has been proposed, leveraging image-based finite element analysis and deep learning techniques [113]. The predictive performance of some of these machine learning models depends on the quality and size of the training dataset. To address limited data in machine learning one can use transfer learning, which utilizes knowledge gained from one problem to solve

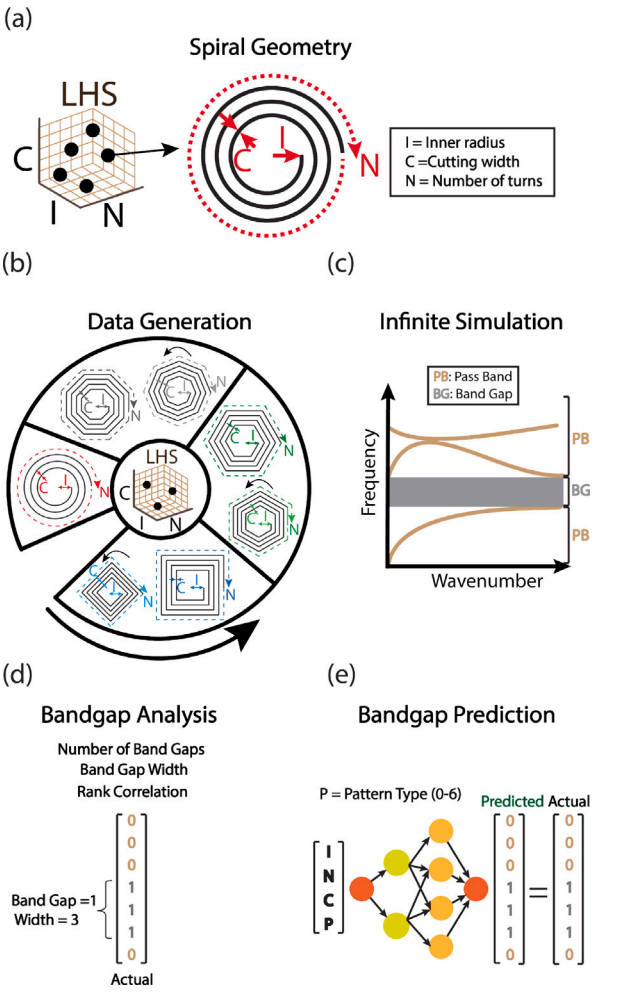

Fig. 1. Concept: (a) An Archimedean spiral with its parameters. (b) Generating datasets to create different spiral shapes using Latin Hypercube Sampling (LHS). (c) Numerically computing the dispersion curves for all the spiral unit cells. (d) Performing band gap analysis, including the number of band gaps, band gap width, and rank correlation, for the proposed unit cells. (e) Predicting band gaps for different spiral geometries using a neural network.

a related problem, offering the benefits of faster convergence and improved prediction accuracy [114–116]

Previous research has focused on single spiral geometries (e.g., Archimedes or Square) and has studied the effect of variations in spiral parameters to compute the phononic band gap for various applications. However, studying and predicting the band gap properties of different complex-shaped spiral resonators remains a challenging issue. The hypotheses for this paper are: (1) there is a similarity between different spiral patterns with respect to the number of band gaps; (2) it is possible to predict the band gap of various spiral patterns; and (3) it is possible to predict the band gap of new spiral types using knowledge from known spiral patterns, even with a limited amount of data for training the ML model. To achieve this, we first generate datasets for various spiral patterns and study their dynamics by numerically computing their dispersion curves. Then, we perform a comparative analysis of these spiral patterns in terms of the number of band gaps, band gap width, and rank correlation. After that, we predict the band gap regions of different spiral geometry unit cells using neural network architectures. Finally, we develop a model for predicting the band gap of new spiral patterns using limited training datasets by transferring knowledge from known spiral patterns.

The remainder of this paper is organized as follows: Section 2 begins with Section 2.1, data generation, followed by Section 2.2 a detailed analysis of the unit cell and Section 2.3 numerical simulations. Section 3 presents an Analysis of similarities in geometry-property relationship across spiral types. Section 4 introduces band gap prediction by leveraging data from different spiral types. Finally, Section 5 concludes the paper.

2. Methodology and computational framework

The proposed framework consists of four steps:

(1) Generating spiral patterns by sampling the parameterized design space (Fig. 1)(b).

(2) Obtaining dispersion curves for all samples through numerical computation (Fig. 1)(c).

(3) Conducting data analysis to understand the similarities in structure–property relationships across various spiral types (Fig. 1)(d).

(4) Validating the hypothesis that data from known spiral types can improve property prediction for new types using transfer learning (Fig. 1)(e).

2.1. Data generation

To generate the data for this study, we create spiral patterns by sampling the parameterized design space defined by cutting width (0.9 to 3), inner radius (0.01 to 0.35), and the number of turns (1 to 10), as shown in Fig. 1(a) using Latin Hypercube Sampling (LHS) [117], while keeping other parameters, such as orientation, outer radius, and unit cell size, fixed. For instance, to generate the Archimedean spiral shape, we use the equation of the spiral which can be written in polar coordinates:

$$r(s) = R - (R - r)s, \;\; \phi(s) = 2\pi n s \tag{1}$$

where r is the inner radius, R is the outer radius, n is the number of turns; in regular polygon-based spirals, each turn of the spiral corresponds to one complete traversal around the polygon. Therefore, the number of sides of the polygon directly relates to the number of turns in the spiral. For instance, a regular polygon with four sides (e.g., a square) will complete one full turn after traversing all four sides.

LHS divides the range of each parameter into N = 60 equally probable intervals, ensuring that each sample covers a unique region of the parameter space:

$$x_{ij} = a_j + u_{ij} \cdot (b_j - a_j) \tag{2}$$

where x_{ij} is the sampled value for parameter j at sample i, a_j and b_j are the lower and upper bounds of the jth dimension, and u_{ij} is a uniformly random number in $[0, 1]$. Instead of random sampling, the center of each interval can be used to generate sample points. In this case, the equation for each point is:

$$x_{ij} = \frac{a_j + b_j}{2} \tag{3}$$

To ensure uniformity, we employed the 'center' criterion, placing samples at the midpoints of these intervals, which promotes an even distribution across each parameter's range. A random permutation of the midpoints across parameters ensures the Latin property, guaranteeing that each interval is sampled exactly once per parameter, thus enhancing representativeness. This approach, visualized in a 3D scatter plot, confirms a uniform and representative distribution of the 60 samples across the parameter space, enabling robust exploration of spiral pattern variations for unit cell design.

To create 60 samples for each spiral pattern, we follow two steps: (1) LHS sample set with shared input parameter values, and (2) LHS sample set with unique input parameter values. This approach allows us not only to study and compare trends across all patterns but also to generate more data. Fig. 2(a) shows that LHS is used to generate 60 sample datasets for each spiral pattern, and one example of each spiral pattern is shown in Fig. 2(b). Additionally, we use the LHS sample set

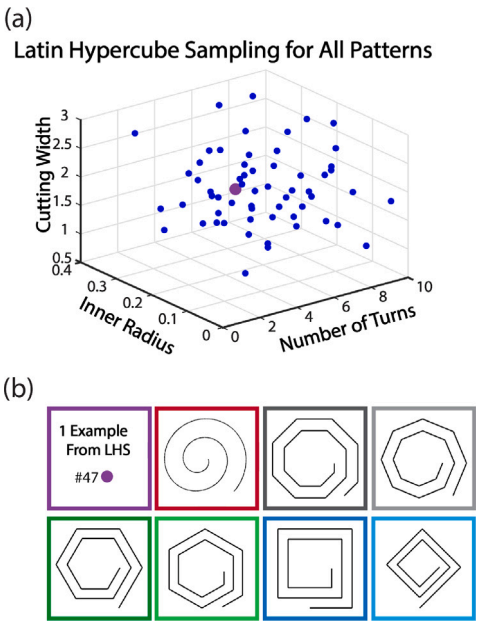

Fig. 2. Generating sixty datasets (a) using LHS sample set with shared input parameters for seven spiral patterns. One example of each pattern is shown inside a unit cell.

with unique input parameter values to generate 60 sample datasets for each spiral pattern, as illustrated in Fig. A.1 in Appendix A. In total, 840 sample datasets are generated using LHS to design the unit cells. Then, we use these sample datasets to generate spiral patterns with MATLAB version R2023b. Finally, we save the output patterns as images for conversion into solid unit cells.

2.2. Unit cell analysis

To study the dynamics of all proposed spiral-based unit cell metamaterials, we assume an infinite repetition of each unit cell in space, implementing a Bloch solution [118] in the following form:

$$\mathbf{u}(\mathbf{x},\kappa;t)=\tilde{\mathbf{u}}(\mathbf{x},\kappa)e^{i(\kappa\cdot\mathbf{x}-\omega t)} \tag{4}$$

where $\tilde{\mathbf{u}}$ represents the Bloch displacement vector, $\mathbf{x}$ is the position vector, κ is the wave number, ω is the frequency, and t is time. By utilizing the Bloch solution, we express the dispersion relation as an eigenvalue problem in the following form:

$$[-\omega^2\mathbf{M}+\mathbf{K}(\kappa)]\boldsymbol{u}=0 \tag{5}$$

where $\mathbf{M}$, $\mathbf{K}$ are the mass and stiffness matrices, respectively. We calculate the dispersion curves, which correlate frequency and wavenumber, for our unit cells by solving the formulated eigenvalue problem. To compute these dispersion curves, we calculated the eigenfrequencies for a given reciprocal wave vector, sweeping along the edge (Γ-X/Y-M-Γ) of the Brillouin zone, using the finite element method in COMSOL Multiphysics version 6.1. Our unit cell is square, with dimensions of $x = y = 10$ mm. The material of the unit cell is acrylic, with a Young's modulus of $E = 3.2026\times10^9$ Pa, density $\rho = 1180$ kg/m^3, and Poisson's ratio $\nu = 0.35$.

2.3. Numerical simulation

To obtain the band structures for all spiral patterns, we first need to convert all 840 images into solid geometry. The workflow for this conversion, including steps (i) to (vi), is illustrated in Fig. A.2(a) in Appendix A. We begin by using the image-to-curve add-in, which allows us to use an image as the starting point for our analysis. Next, we generate an interpolation curve from a contour plot of the imported image using the add-in. This curve can then serve as a component within the geometry. Afterward, we add a solid square unit cell and use the Difference tool to subtract the solid spiral from the unit cell. Finally, we create a mesh for the unit cell. The finer mesh leads to higher computational time and can also impact the accuracy of the predicted band gap [119–121]. Therefore, depending on the problem and geometry type, we employ an appropriate meshing technique. In this study, we examine pixel and conformal meshes and select the technique that provides the most accurate dispersion curves. The conformal mesh proves to be the most effective, as shown in Fig. A.2(b–c).

We numerically compute the dispersion curves of the 840 spiral geometries created in the previous step. An example of the numerically computed dispersion curves for selected patterns from Fig. 2(b) is shown in Fig. 3. To further analyze and utilize all the output data, we normalize the frequency on the dispersion curves using the following equation:

$$f_{\text{normalized}}=\frac{f-\min(f)}{\max(f)-\min(f)} \tag{6}$$

where f is original eigenfrequency values, $\min(f)$ is the minimum value in the dataset, and $\max(f)$ is the maximum value in the dataset. The color-coded vector next to each dispersion curve indicates the pass band, highlighted in blue, while the magenta-shaded region highlights the frequency ranges of the band gaps. We discretize the vector into 0 s and 1 s, representing the pass bands and band gaps, respectively, with an increment of 0.1. It is important to note that if the frequency range between two adjacent band gaps is very close, the band gaps are merged. This simplification facilitates tracking all the bands for further analysis and predictions.

3. Analysis of similarities in geometry-property relationship across spiral types

After computing the dispersion curves for all the proposed spiral patterns, our goal is to obtain a quantitative understanding of the similarities in the geometry-property relationship across various types of spirals and quantify the similarities using Spearman's rank correlation coefficient [122]. This coefficient quantifies the degree of association between two ranked variables by comparing their ranks rather than their actual values. To guide metamaterial design effectively, we use rank correlation because it allows us to assess the relationships between geometric features such as spiral shape and their corresponding material properties like band gap counts and widths without being influenced by outliers or the specific values of the properties. We examine the correlation between band gap counts and band gap widths to understand how these characteristics relate among the various spiral patterns using the following equation:

$$\rho=1-\frac{6\sum_{i=1}^{n}d_i^2}{n(n^2-1)} \tag{7}$$

where d_i is the difference between the ranks of each pair of values, and n is the number of observations. The coefficient, denoted by ρ, ranges from -1 to 1. A value of $\rho = 1$ indicates a perfect positive correlation, $\rho = -1$ indicates a perfect negative correlation, and $\rho = 0$ indicates no correlation. To count the number of band gaps and calculate the band gap width, we use the following equations:

$$C=\sum_{i=1}^{n}I(b_i) \tag{8}$$

where $I(b_i)$ is an indicator function that returns 1 if a band gap is present and 0 otherwise.

$$W=f_{\text{end}}-f_{\text{start}} \tag{9}$$

where f_{end} and f_{start} are the frequencies at the end and start of the band gap, respectively.

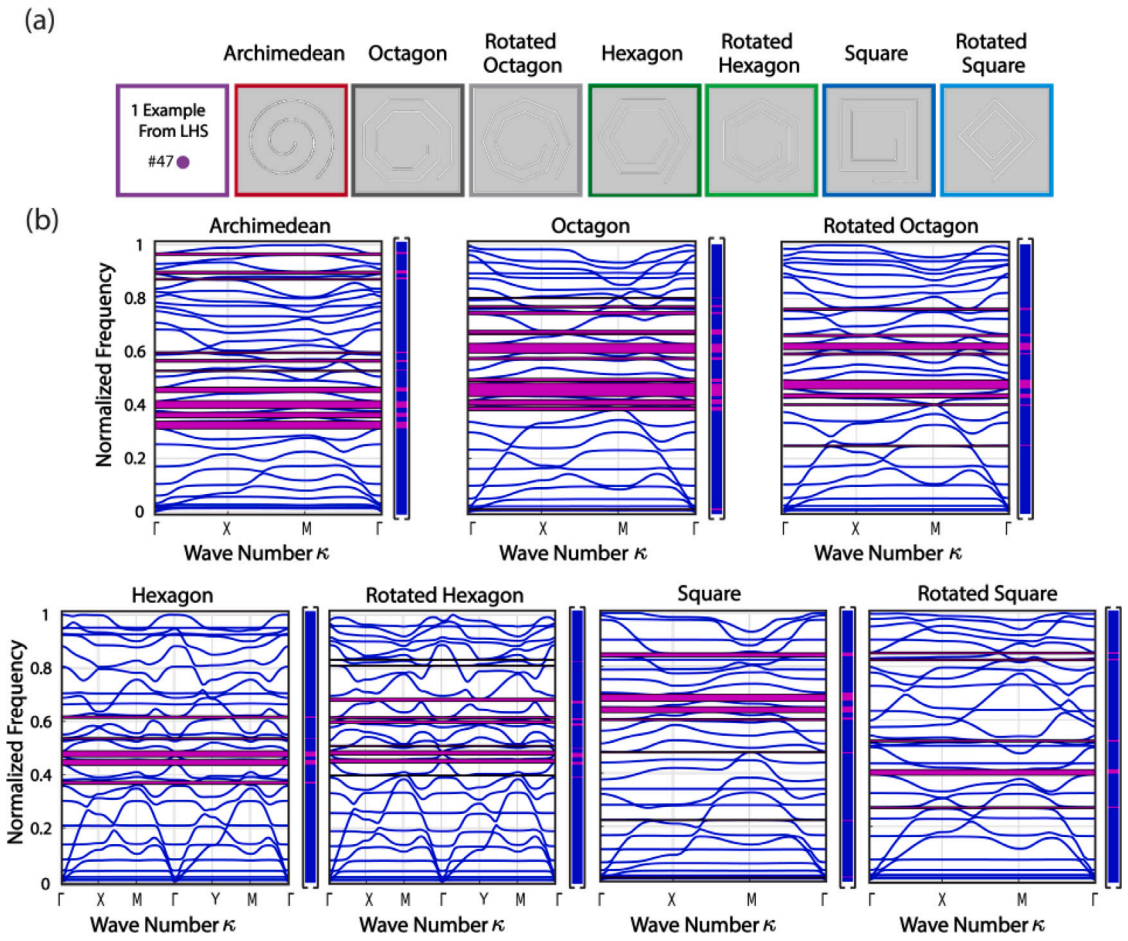

Fig. 3. Example of (a) unit cells with different spiral geometries created from the same LHS. (b) Numerically computed dispersion curves for infinitely repeated unit cells. The frequency of all dispersion curves is normalized to provide consistent output for further analysis. The color-coded vectors for each dispersion curve, shown next to each plot, represent pass bands and band gap details. These vectors are later discretized for band gap detail analysis and band gap prediction. Each dispersion curve indicates the pass band, highlighted in blue, while the magenta-shaded regions highlight the frequency ranges of the band gaps. (For interpretation of the references to color in this figure legend, the reader is referred to the web version of this article.)

The Spearman's rank correlation is computed for both band gap counts Fig. 4(a) and widths Fig. 4(b) for seven distinct geometric patterns: Archimedean spiral, octagon, rotated octagon, hexagon, rotated hexagon, square, and rotated square. These correlation coefficients provided a quantitative basis to assess the degree of similarity in band gap characteristics between different geometrical structures. The analysis shows strong positive correlations in band gap counts among most geometrical patterns. The Archimedean spiral and octagon exhibit a strong positive correlation of $\rho = 0.87$, suggesting synchronized occurrence of band gaps despite their differing geometries. In contrast, the highest correlation of $\rho = 0.96$ between the rotated octagon and octagon indicates that rotation minimally affects band gap counts. Suggesting that the symmetry in pattern contributes to stable band gap formation. Similarly, the hexagon and rotated hexagon show a high correlation of $\rho = 0.86$, implying that geometric rotation has limited effects on band gap counts in hexagonal structures. The square and rotated square also demonstrate a significant correlation of $\rho = 0.83$, reinforcing the idea that rotations minimally influence band gap occurrences. The correlation $\rho = 0.84$ between the rotated hexagon and rotated square suggests a close relationship in their band gap counts, despite their differing geometries. Notably, the correlation $\rho = 0.88$ between the octagon and hexagon reflects a strong similarity in band gap behavior, despite their different side counts. Lastly, the strong correlation of $\rho = 0.90$ between the Archimedean spiral and rotated octagon shows a strong positive relationship, which is notable given the structural differences between these shapes.

In contrast to the band gap counts, the reordered Spearman's rank correlation matrix for band gap widths reveals more diverse relationships. The negative correlation of $\rho = -0.024$ between the Archimedean spiral and octagon suggests that, despite similar band gap counts, the widths of the band gaps differ considerably. Similarly, the low correlation of $\rho = 0.013$ between the rotated octagon and octagon further indicates that while band gap counts are nearly identical, their widths are not closely aligned. A negative correlation of $\rho = -0.10$ between the hexagon and rotated hexagon indicates that the band gap widths are inversely related, and even slight geometric rotation can significantly affect band gap width distribution. In contrast, the positive correlation of $\rho = 0.23$ between the rotated hexagon and rotated square indicates similarities in band gap widths distribution, despite their different shapes. Similarly, a correlation of $\rho = 0.21$ between the octagon and hexagon suggests that, despite structural differences, they also share similarities in band gap width distribution. Additionally, the moderate positive correlation of $\rho = 0.18$ between the Archimedean spiral and hexagon suggests some alignment in band gap widths, despite their distinct structures. Lastly, the negative correlation of $\rho = -0.041$ between the square and rotated square indicates that while their band gap counts are close, rotation significantly impacts width distribution.

We observed that geometric rotation minimally impacts band gap counts across similar patterns, such as a rotated octagon and octagon. The Archimedean spiral, despite not being a polygon-based spiral, exhibits a high correlation and shares certain geometric properties

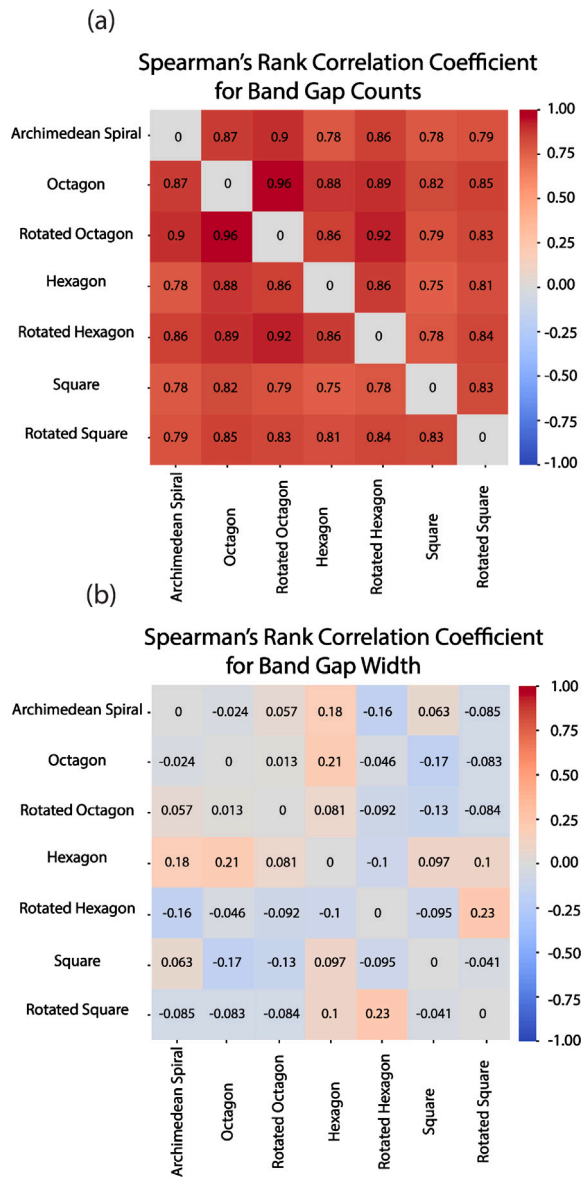

Fig. 4. Spearman's Rank correlation coefficient analysis. (a) Correlation between band gap counts and (b) correlation between band gap widths. These heat maps visualize the strength and direction of monotonic relationships between band gap counts and their widths, with color intensity representing the degree of correlation. (For interpretation of the references to color in this figure legend, the reader is referred to the web version of this article.)

regarding band gap counts with all patterns. Polygon-based spirals, like the octagon and hexagon, demonstrate a high correlation despite their differing geometries and number of sides.

However, band gap widths exhibit greater variability between patterns, suggesting that structural differences, such as shape (change in spiral parameters) and rotation, play a more significant role in determining gap widths. Overall, while polygon-based spirals show a correlation in band gap counts, they exhibit minimal or even inverse correlation in band gap widths, with only a moderate correlation observed between the hexagon and octagon. Despite not being a polygon-based spiral, the Archimedean spiral shows minimal or inverse correlation in band gap widths with all patterns, except for the hexagon.

The weak correlation observed in band gap width can be attributed to the complex influence of geometric parameters on the band structure. Specifically, changes in parameters such as the number of turns, inner radius, and cutting width significantly affect both the position and width of the band gaps. For example, increasing the number of turns while keeping other parameters constant tends to shift the band gaps to lower frequencies and reduce their width, while decreasing the number of turns has the opposite effect. Similarly, reducing the inner radius results in a higher frequency shift and an increase in band gap width, whereas increasing the inner radius lowers the band gap frequency and narrows the width. Adjusting the cutting width also impacts the band gap characteristics: a larger cutting width shifts the band gap to lower frequencies and narrows the width, while a smaller width raises the band gap frequency and broadens it. It should be noted that the shift in band gap frequency is primarily due to changes in the effective stiffness within the core of the unit cells. Altering the geometric parameters modifies the internal structure, thereby affecting the local stiffness and consequently the dynamic response of the unit cell. Despite these variations in band gap position and width, the total number of band gaps tends to remain relatively similar or close across different geometries, which explains the stronger correlation observed in band gap count.

4. Band gap prediction by leveraging data from different spiral types

After analyzing the correlations among all spiral patterns, we confirm our hypothesis that similarities exist between them. This section aims to demonstrate the feasibility of leveraging data of known spiral types to enhance the prediction accuracy of band gaps of new spiral types.

4.1. General idea of neural network models

Building on the insights gained from our analysis of the correlations among spiral patterns, we establish different neural network models to predict their band gaps. To do this, we start with two models: Baseline 1 (B1) and Baseline 2 (B2). We use the B1 model to train on all seven spiral patterns, totaling 840 datasets (see Fig. 5(a)). For the B2 model, we use the same neural network to train on three spiral types of interest: (i) Archimedean, (ii) Octagon, and (iii) Square. Each pattern has 120 datasets, as illustrated in Fig. 5(b). To enhance the accuracy of the band gap prediction, we first employ Transfer Learning Preliminary (TLP) to train on data excluding the spiral types of interest (see Fig. 5(c)(i–iii)). We then introduce Transfer Learning (TL) model to train on small datasets of 120 for each spiral type of interest (i–iii). This model leverages knowledge from the different spiral configurations to enhance the band gap prediction of unknown spiral patterns. The models include an input layer that consists of specific parameters of spiral geometry, such as cutting width, inner radius, and the number of turns, as shown in Fig. 1(a). Additionally, we have included one extra variable labeled as pattern type, which ranges from 0 to 6, ensuring representation of each pattern type in both the training and testing sets. Detailed descriptions of the B1, B2, and TL models' architectures and training procedures are provided in Appendix B.

Data preparation involves normalizing the input data using Min–Max scaling:

$$X_{\text{norm}} = \frac{X - X_{\min}}{X_{\max} - X_{\min}} \tag{10}$$

where X is the original feature value, $X_{\min}$ and $X_{\max}$ are the minimum and maximum values of the feature in the datasets, respectively. It ensures all features contribute equally by scaling them to the same range. The neural network architecture includes six dense layers with ReLU activation functions as hidden layers. Batch normalization and dropout layers are applied after each dense layer to enhance generalization and prevent overfitting. For the output, we focus on quantifying and comparing consecutive sequences of positive instances, referred to as band gaps, in binary classification datasets. The process involves

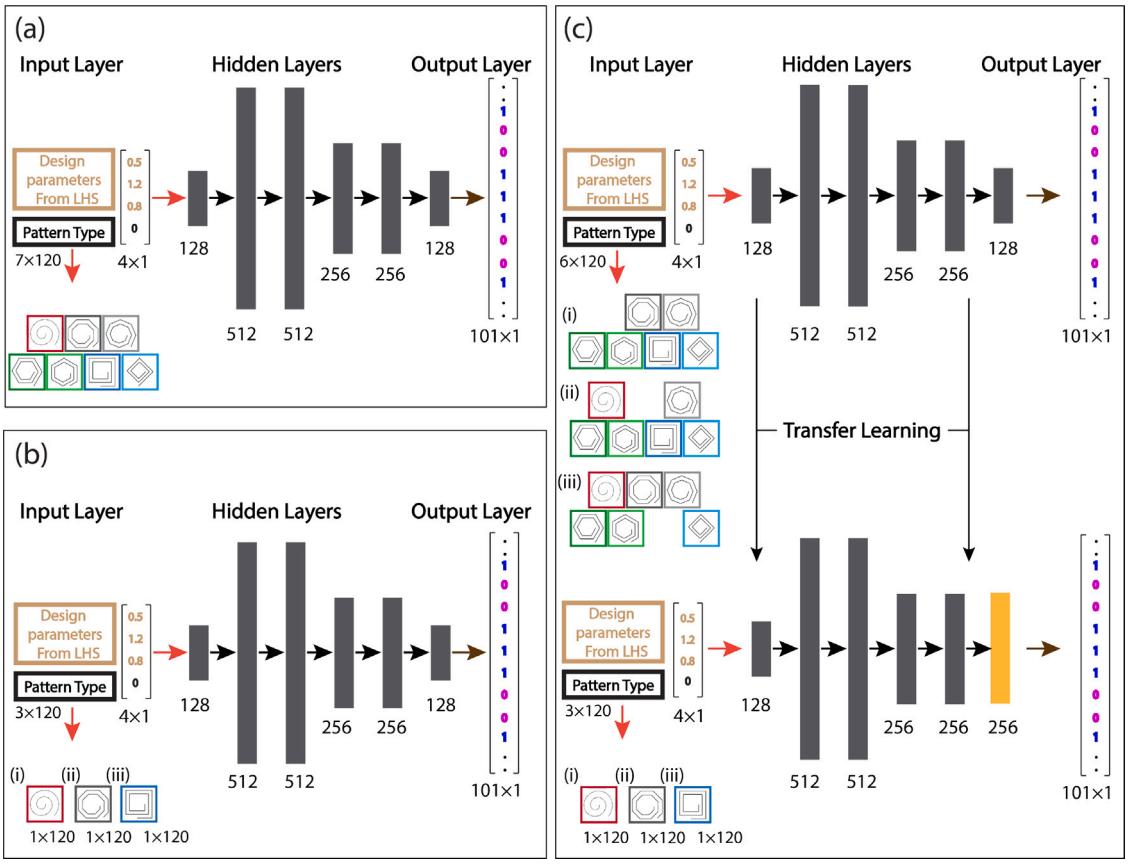

Fig. 5. Architecture of three neural network models. (a) Baseline 1 (B1): This model is trained using seven different spiral patterns, each with 120 data points, resulting in a total of 840 datasets. (b) Baseline 2 (B2): This model is trained separately on three spiral types of interest: (i) Archimedean, (ii) Octagon, and (iii) Square, with each having 120 datasets. (c) Transfer Learning preliminary (TLP): The model is trained in three separate steps: (i) on all spiral patterns excluding Archimedean (720 datasets in total), (ii) on all spiral patterns excluding Octagon (720 datasets in total), and (iii) on all spiral patterns excluding Square (720 datasets in total). Transfer Learning (TL): Transferring knowledge from the TLP model to the TL model to enhance the accuracy of the band gap prediction for three spiral types of interest using limited training data (each having 120 datasets). In the transfer learning model, all layers of the trained model are frozen except the last one, where a new layer is added and trained as the final layer. For each model, 80% of the data is used for training and 20% is used for testing for each pattern.

counting these band gaps separately for actual and predicted data. For the actual data, we identify sequences of consecutive 1 s by traversing through indices where the true values are 1. We count the length of each sequence to determine the number of band gaps. Similarly, for the predicted data, we analyze the predicted 1 s and their overlap with actual 1 s to count the number of predicted band gaps. By comparing these counts, we evaluate the model's accuracy in detecting and predicting consecutive sequences of positive instances, providing insight into the model's performance and areas for improvement. For training the neural network, we use a batch size of 64 and train for 2000 epochs.

4.2. Specific test cases

To predict the band gaps of all spiral patterns, we set up our computational experiments as follows. In model B1, we allocate 80% of the datasets for training and 20% for testing for each of the seven known spiral patterns. For model B2, we consider 80% of the datasets for training and 20% for testing for three known spiral types of interest: (i) Archimedean, (ii) Octagon, and (iii) Square. Furthermore, we introduce three TLP models to predict band gaps of various spiral patterns. The first model trains on six known spiral patterns, excluding Archimedean; the second model trains on six known spiral patterns, excluding Octagon; and the third model trains on six known spiral patterns, excluding Square. In all three models, we allocate 80% of the datasets for training and 20% for testing for each spiral pattern. To improve the accuracy of the band gap predictions, we transfer five layers from TLP model to the TL model and discard the last layer. Only the newly added layer is trainable. These steps allow us to transfer knowledge from known spiral patterns to enhance the accuracy of the band gap prediction of three unknown spiral patterns: (i) Archimedean, (ii) Octagon, and (iii) Square.

Table 1
Performance of three different models in predicting the validation set for Archimedean spirals.

Performance metric	Baseline 1	Baseline 2	TL
Accuracy	0.917	0.910	0.908
Recall	0.439	0.418	0.538
Precision	0.593	0.544	0.518
F1 score	0.504	0.473	0.528

4.3. Results of test cases

To evaluate the performance of our neural network models, we employ several metrics and visualizations on the test set. We calculate accuracy, recall, precision, and the F1 score to assess classification performance [123]. Accuracy provides a measure of overall correctness, while recall and precision assess the model's ability to identify positive instances. The F1 score combines these metrics into a single value that balances precision and recall.

Our analysis shows the comparative performance of three different models, B1, B2, and TL, on predicting validation sets for three spiral

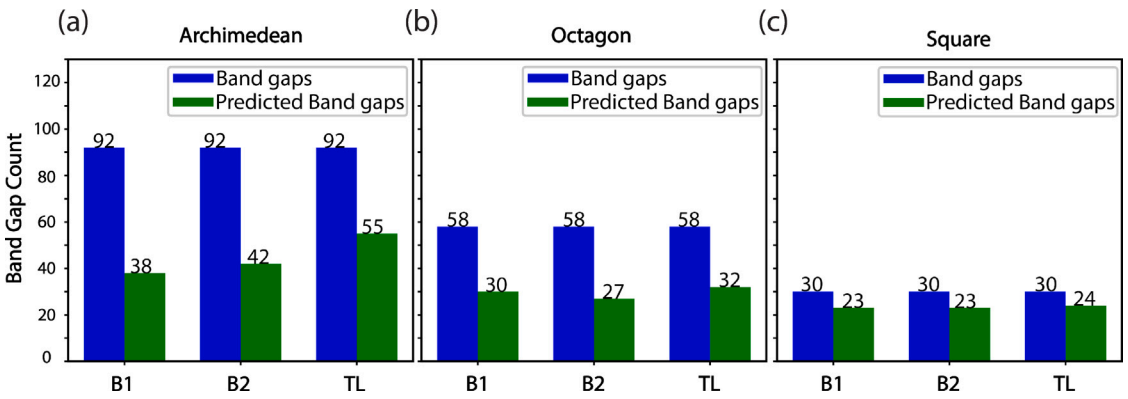

Fig. 6. Band gap prediction based on three models: Baseline 1 (B1), Baseline 2 (B2), and Transfer Learning (TL) for: (a) Archimedean spirals, (b) Octagon spirals, and (c) Square spirals.

Table 2
Performance of three different models in predicting the validation set for Octagon spirals.

Performance metric	Baseline 1	Baseline 2	TL
Accuracy	0.925	0.916	0.941
Recall	0.337	0.377	0.516
Precision	0.389	0.343	0.530
F1 score	0.361	0.359	0.523

Table 3
Performance of three different models in predicting the validation set for Square spirals.

Performance metric	Baseline 1	Baseline 2	TL
Accuracy	0.989	0.980	0.989
Recall	0.650	0.620	0.750
Precision	0.680	0.540	0.652
F1 score	0.660	0.580	0.697

types of interest: Archimedean spirals (Table 1), Octagon spirals (Table 2), and Square spirals (Table 3). In each table, B1 and B2 focus on general prediction accuracy for known spirals, while TL is designed to predict accuracy for unknown spirals. For the Archimedean spiral pattern, as shown in Table 1, the TL model performs slightly better than B1 and B2 in terms of F1 score, achieving a value of 0.528 compared to B1's 0.504 and B2's 0.473. While the accuracy of TL is marginally lower than B1 for known spirals, it outperforms in recall (0.538) and F1 (0.528). This suggests that, although B1 has the highest accuracy (0.917) for known spirals, TL shows a more balanced performance across recall, precision, and F1 score. This indicates its robustness in handling both false positives and false negatives when predicting unknown spirals.

For Octagon spirals, Table 2 indicates that TL again achieves superior results for unknown spirals, with the highest F1 score of 0.523, compared to B1 (0.361) and B2 (0.359) for known spirals. TL also excels in recall (0.516) and precision (0.530), suggesting better predictive capability for this pattern type among unknown spirals. The accuracy values for all models are comparable, with TL slightly outperforming the other models at 0.941. For Square spirals, both B1 and TL exhibit identical accuracies of 0.989 for known and unknown spirals, respectively, indicating that they predict the same number of correct instances overall. However, TL significantly outperforms B1 and B2 in recall (0.750) and F1 score (0.697) for unknown spirals, suggesting that TL is more effective at identifying true positive instances, while also maintaining strong performance in identifying true negatives, particularly those that are harder to detect.

Across all three tables, the TL model consistently demonstrates strong performance in identifying unknown spirals. While B1 occasionally achieves higher accuracy for known spirals, TL's balanced results in recall, precision, and F1 score indicate superior pattern recognition. Additionally, TL's robust feature learning from pre-trained models enhances its ability to generalize across various geometrical patterns, making it a more reliable choice for predicting band gaps.

The band gap prediction results for the Archimedean spiral, as shown in Fig. 6(a), indicate that the actual number of band gaps is 92. B1 and B2 underperform significantly, with B1 predicting 38 band gaps and B2 slightly better at 42 for known spirals. In contrast, the TL model demonstrates stronger predictive power by identifying 55 band gaps for unknown spirals. Although this still falls short of the actual count, TL shows a clear improvement over B1 and B2, highlighting its superior ability to capture the underlying patterns in this dataset. For the Octagon spiral, illustrated in Fig. 6(b), the models again show varying levels of prediction accuracy. The actual number of band gaps is 58. B1 predicts 30 band gaps, while B2 is slightly lower at 27, both of which considerably underpredict for known spirals. TL performs better, predicting 32 band gaps for the unknown spirals, demonstrating its effectiveness in this context. In the case of the Square spiral, the actual number of band gaps is 30, as illustrated in Fig. 6(c). Both B1 and B2 predict 23 band gaps for known spirals. TL, on the other hand, performs better, predicting 24 band gaps and coming closest to the actual value. Here, the predictions made by all three models are relatively close to the actual count, with TL demonstrating the highest degree of accuracy. Overall, these results indicate that while B1 and B2 excel in accuracy for known spirals, the TL model is the most effective in balancing prediction accuracy with recall and precision for unknown spirals. This comparison underscores the importance of evaluating multiple metrics when selecting a model for predictive tasks, particularly when handling geometrically complex patterns like spirals.

We also analyze the percentage of band gap predictions across different models for the spiral types of interest: Archimedean, Octagon, and Square. The results indicate that 20% of the hidden test sets are used for both known and unknown spiral patterns, as shown in Fig. 7. For the Archimedean spirals (Fig. 7(a)), B1 accurately predicts 100% of the band gaps in 13 cases, with a total of 15 predictions exceeding 50% accuracy and 9 falling below 50%. B2 demonstrates slightly better performance, predicting 100% of the band gaps in 14 cases, with a total of 15 predictions above 50% accuracy and 9 below 50%. The TL model performs best, achieving 100% prediction accuracy in 14 cases, with 18 predictions above 50% and only 6 below 50% for unknown spirals. For the Octagon spirals (Fig. 7(b)), B1 correctly predicts 100% of the band gaps in 14 cases, with 17 predictions exceeding 50% accuracy and 7 below 50%. B2 achieves 100% accuracy in 12 cases, with 15 predictions above 50% and 9 below 50%. Once again, the TL model outperforms the others, achieving 100% prediction accuracy in 15 cases, with 18 predictions above 50% and 6 below 50%. This reinforces TL's capability to predict unknown spirals effectively. In the case of the Square spirals (Fig. 7(c)), both B1 and B2 successfully predict 100%

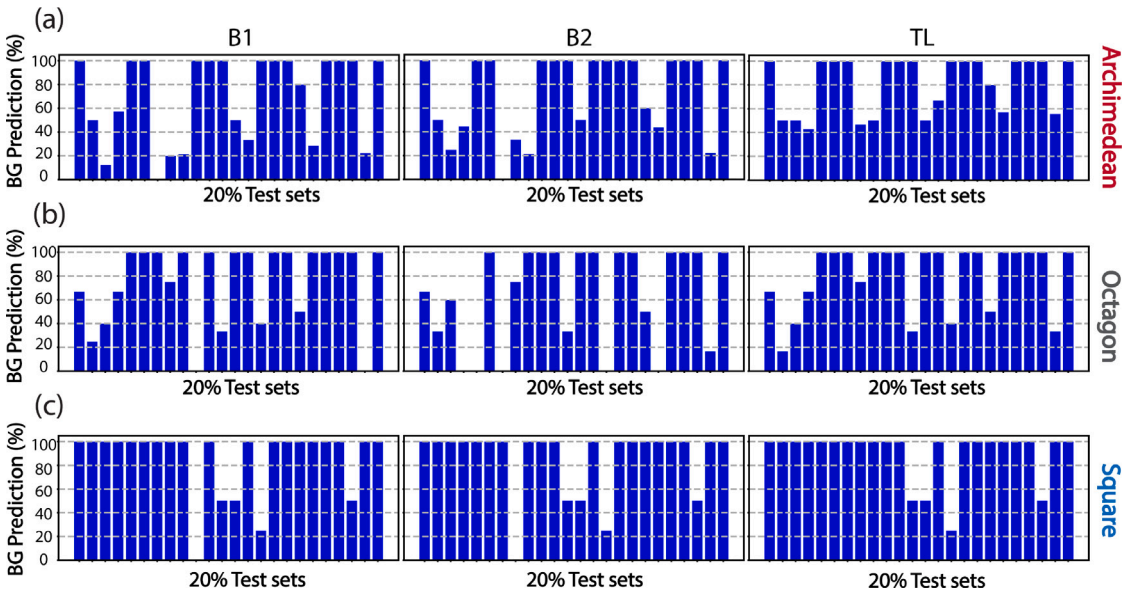

Fig. 7. Percentage of band gap prediction in different models: Baseline 1 (B1), Baseline 2 (B2), and Transfer Learning (TL) for three spiral types of interest: (a) Archimedean, (b) Octagon, and (c) Square. The results show 20% of hidden test sets data for both known (B1 and B2) and unknown (TL) spiral patterns.

of the band gaps in 19 cases, with all 19 predictions exceeding 50% accuracy and only 5 predictions below 50% for known spirals. The TL model shows strong performance with 100% accuracy in 20 cases, with 20 predictions exceeding 50% accuracy and only 4 predictions below 50% for unknown spirals.

It is worth noting that in the B1 and B2 models, there are instances across all three spirals where the models are unable to predict any band gaps for some datasets. In contrast, the TL model demonstrates better performance by successfully predicting those band gaps that are missed by B1 and B2, highlighting its robustness in dealing with unknown spirals.

The superior performance of the TL model can be attributed to its ability to reuse abstract feature representations learned from related spiral geometries during the preliminary phase. These features, such as the influence of spiral parameters on the band gap, allow the model to generalize better to unseen spiral types, even with limited training data. This capability is particularly critical in phononic metamaterials, where generating large datasets through finite element simulations is computationally expensive. By transferring knowledge from a related but different task, TL captures nuanced structural-property relationships, such as variations in band gap width, which are often missed by models (B1 and B2) trained from scratch. Furthermore, in practical applications like wave filtering or vibration isolation, TL's ability to accurately predict band gaps with minimal data makes it a highly efficient tool for the rapid design of novel metamaterial structures.

5. Conclusions

This study provides a comprehensive analysis of band gap properties in phononic metamaterials featuring various spiral geometries, specifically Archimedean, Octagon, Hexagon, and Square spirals. By generating synthetic data for these spiral patterns and conducting extensive computational analyses, we examine key aspects such as band gap width, count, and rank correlation. Our findings reveal that Archimedean spirals have a high correlation with all spiral patterns in terms of band gap counts. Notably, the correlation between band gap widths for different spiral geometries is less consistent, reflecting how variations in geometry can affect the distribution of band gaps across the frequency spectrum. The Spearman's rank correlation analysis highlights that geometric rotation has minimal impact on band gap counts. In addition to our analysis, we leverage knowledge from known spiral patterns to improve the prediction accuracy of band gaps for new types of spirals. The findings highlight that the TL model consistently demonstrates superior predictive accuracy and a better grasp of underlying patterns for unknown spiral patterns compared to B1 and B2 across different known spiral patterns. While B1 and B2 tend to significantly underpredict the number of band gaps, the TL model exhibits a more refined understanding of the data, leading to predictions that are closer to the actual values, even with a small dataset. This indicates that TL's approach is more adept at capturing the complexities of the dataset and providing more reliable predictions, especially in scenarios where precise pattern recognition is crucial. Overall, this research underscores the critical role of geometric patterns in influencing the dynamic properties of phononic metamaterials. By offering a detailed comparison of various spiral geometries and their effects on band gap characteristics, our study provides valuable insights that can guide the design and optimization of phononic materials. This contribution paves the way for more targeted and efficient applications in wave manipulation.

CRediT authorship contribution statement

Majid Kheybari: Writing – review & editing, Visualization, Software, Investigation, Data curation, Writing – original draft, Validation, Methodology, Formal analysis. **Hongyi Xu:** Writing – original draft, Resources, Funding acquisition, Writing – review & editing, Supervision, Project administration, Conceptualization.

Declaration of competing interest

The authors declare the following financial interests/personal relationships which may be considered as potential competing interests: Hongyi Xu reports financial support was provided by National Science Foundation. If there are other authors, they declare that they have no known competing financial interests or personal relationships that could have appeared to influence the work reported in this paper.

Acknowledgments

HX gratefully acknowledge financial support from the National Science Foundation, United States (CAREER Award CMMI-2142290).

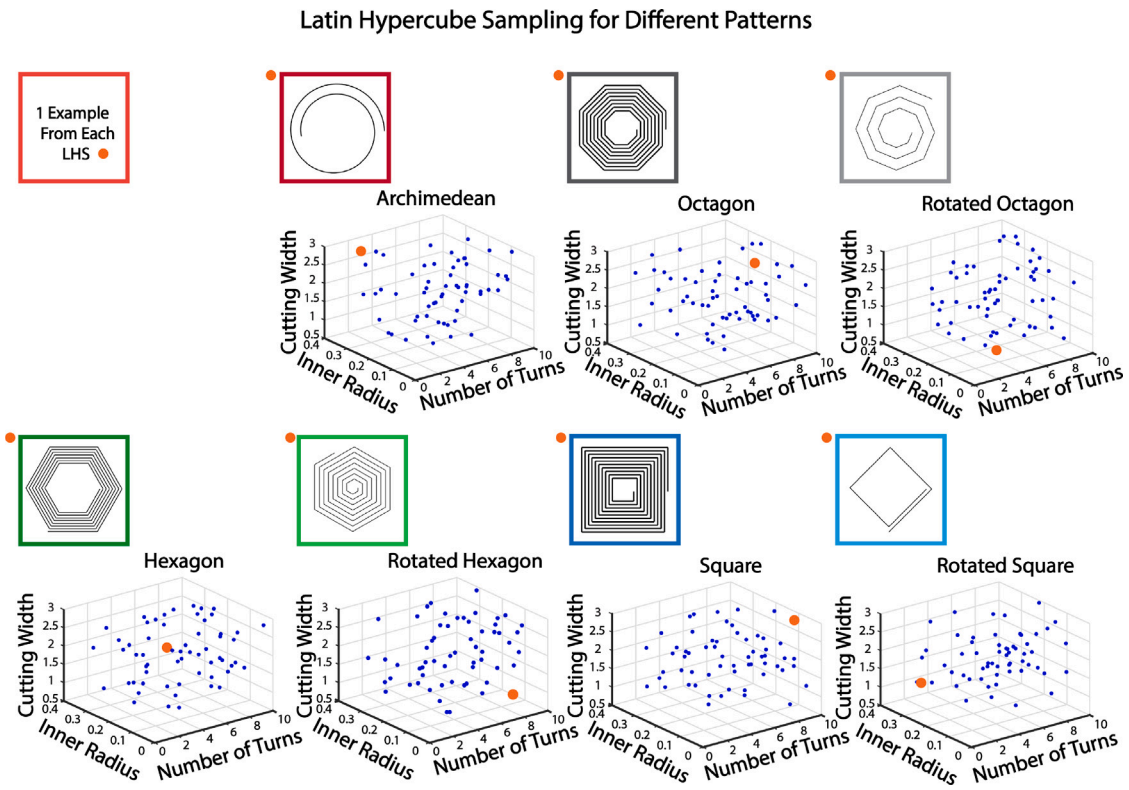

Fig. A.1. Generating sixty datasets using LHS sample set with unique input parameter values for seven spiral patterns. One example of each pattern is shown inside a unit cell.

Appendix A. Data generation, workflow, and mesh selection for spiral geometries

We use LHS sample set with unique input parameter values to generate 60 sample datasets for each spiral pattern. Fig. A.1 shows one example of each spiral pattern generated using LHS sample set with unique input parameter values.

Fig. A.2 shows the workflow for converting an image to solid geometry and selecting the appropriate mesh type for the proposed spiral geometries. To select the appropriate mesh type for the generated spiral geometries, we analyze various meshing techniques and compare their effectiveness. We first start by analyzing the dyanmics of the unit cell that has rectilinear geometry, as shown in Fig. A.2(b). We analytically and numerically compute the dispersion curves for the cross or plus geometry using two different meshing techniques: pixel and conformal. We obtain Similar dispersion curves for both methods, as shown in Fig. A.2(b) (I) and (II). The question now arises: can we achieve the accurate results for non-rectilinear geometries using the same methods? Next, we consider the spiral pattern and repeat the simulations using both meshing techniques. The results show that (I) there is a discrepancy in the dispersion curves when using the pixel mesh, as it fails to capture all areas of the curved pattern, which alters the cutting width within the spiral geometry and impacts the dispersion branches. However, (II) the conformal mesh captures more details, resulting in more accurate dispersion curves, as shown in Fig. A.2(c)

Appendix B. Machine learning models

B.1. Baseline 1 (B1)

The neural network consists of six fully connected hidden layers with varying sizes: 128 units in the first and last layers, 512 units in the second and third layers, and 256 units in the fourth and fifth layers. Each hidden layer is followed by a Batch Normalization and a Dropout (with a rate of 0.3) to enhance training stability and mitigate overfitting. The ReLU activation function is used in all hidden layers to introduce non-linearity, while the output layer employs the sigmoid activation function to independently produce probabilities for each of the 101 output labels. The model is compiled using the binary cross-entropy loss function and optimized with the Adam optimizer at an initial learning rate of 0.001. A batch size of 64 and up to 2000 training epochs were used to ensure full convergence. The input to the neural network consists of 4 features per sample – three scaled using Min–Max normalization and one categorical pattern type – while the output consists of 101 binary labels, representing a multi-label classification problem across 840 total samples.

B.2. Baseline 2 (B2)

The neural network consists of six fully connected hidden layers with varying sizes: 128 units in the first and last layers, 512 units in the second and third layers, and 256 units in the fourth and fifth layers. Each hidden layer is followed by a Batch Normalization and a Dropout (with a rate of 0.3) to stabilize training and reduce overfitting. The ReLU activation function is used throughout all hidden layers to introduce non-linearity, while the output layer uses a sigmoid activation function to independently predict probabilities for each of the 101 output labels. The model is compiled with the binary cross-entropy loss function and optimized using the Adam optimizer with an initial learning rate of 0.001. Training is conducted with a batch size of 64 over up to 2000 epochs. The input to the neural network consists of 3 features per sample, scaled using Min-Max normalization, and the output consists of 101 binary labels per sample, forming a multi-label classification task across 120 total samples.

B.3. Transfer Learning (TL)

We train a preliminary model on 720 samples of known spiral, the model consists of six fully connected hidden layers with varying sizes:

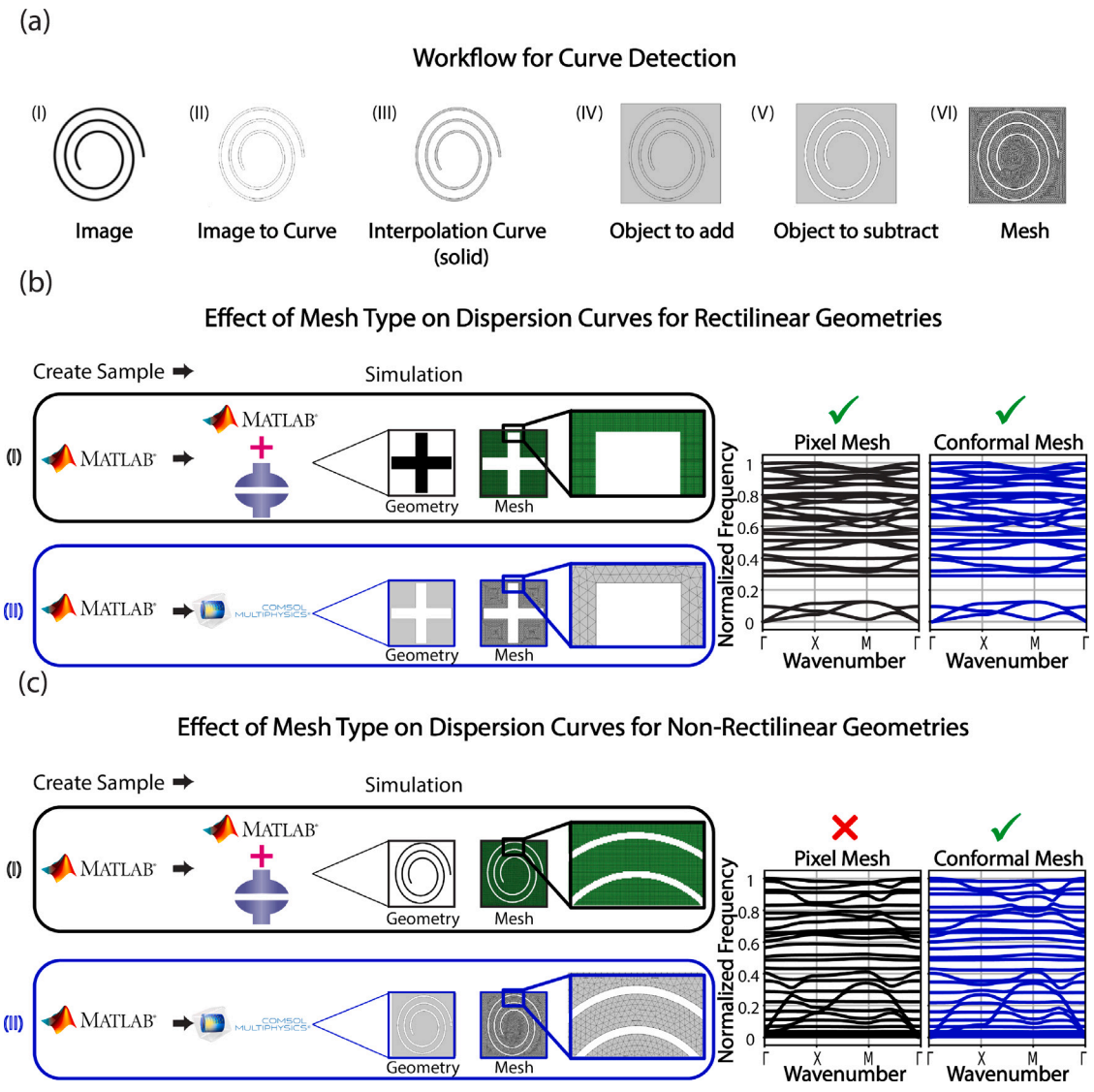

Fig. A.2. (a) Workflow for converting an image to solid geometry. The proposed framework includes appropriate mesh selection for computing dispersion curves. It examines the effect of mesh type on dispersion curves using (b) rectilinear geometries and (c) non-rectilinear geometries. The dispersion curves using both pixel and conformal meshes are consistent for rectilinear geometry, while there is a discrepancy between the dispersion curves for non-rectilinear geometry when using pixel and conformal meshes.

128 units in the first and last layers, 512 units in the second and third layers, and 256 units in the fourth and fifth layers. Each hidden layer is followed by a Batch Normalization and a Dropout (with a rate of 0.3). The ReLU activation function is used throughout all hidden layers. Training is carried out with a batch size of 64 for up to 2000 epochs. The input to the neural network consists of 4 features per sample: three scaled using Min–Max normalization and one pattern type, and the output consists of 101 binary labels per sample, forming a multi-label classification task across 720 total samples. For the transfer learning approach, we adapt a pre-trained preliminary model to a new dataset of 120 samples. The new input data includes 4 features per sample: three scaled using Min–Max normalization and one pattern type, while the output remains a multi-label classification task with 101 binary labels per sample. To retain previously learned feature representations, the pre-trained model is transferred by setting all layers as non-trainable, except the last layer before the output, which is removed and replaced with new layers: a dense layer with 256 units, followed by Batch Normalization and a Dropout layer with a rate of 0.3. The output layer, a sigmoid-activated dense layer with 101 units remains structurally the same as in the original model to maintain compatibility with the multi-label task. Training on the new dataset is also conducted with a batch size of 64 for up to 2000 epochs, allowing the model to fine-tune on the new data while preserving the generalized structure learned from the original dataset.

Data availability

Data will be made available on request.

References

[1] X. Wang, Z. Liang, Z. Tang, S. Rui, K. Li, F. Ma, On-demand design for elastic metamaterial based on a semi-analytical band gap rapid extraction method, Mater. Horizons (2025).

[2] G. Comandini, M. Ouisse, V. Ting, F. Scarpa, Architected acoustic meta-materials: An integrated design perspective, Appl. Phys. Rev. 12 (1) (2025).

[3] Y. Bao, Z. Jia, Q. Tian, Y. Luo, X. Zhang, Z. Kang, Phononic crystal-based acoustic demultiplexer design via bandgap-passband topology optimization, Compos. Struct. 351 (2025) 118622.

[4] J. Jing, P. Sun, Z. Wu, F. Li, Investigation on enhanced band-gap properties of 2D hierarchical phononic crystals, Mech. Syst. Signal Process. 223 (2025) 111827.

[5] W. Huang, J. Xu, Y. Yao, Y. Zhang, X. Wang, P. Han, Application of phononic crystals in modern engineering vibration and noise control, a review, Noise Vib. Worldw. (2025) 09574565251333071.
[6] I. Arretche, K.H. Matlack, Locally resonant effective phononic crystals for subwavelength vibration control of torsional cylindrical waves, J. Vib. Acoust. 144 (3) (2022) 031007.
[7] Y. Achaoui, V. Laude, S. Benchabane, A. Khelif, Local resonances in phononic crystals and in random arrangements of pillars on a surface, J. Appl. Phys. 114 (10) (2013).
[8] Y. Qiu, J. Li, Z. Song, A novel active switchable multi-channel waveguide based on the bragg scattering mechanism and the force-magnetic coupling effect, Multidiscip. Model. Mater. Struct. (2025).
[9] W. Ding, D. Tang, Y. Liu, L. Chen, X. Sun, Compact and low crosstalk waveguide crossing using impedance matched metamaterial, Appl. Phys. Lett. 96 (11) (2010).
[10] V. Laude, Principles and properties of phononic crystal waveguides, Apl Mater. 9 (8) (2021).
[11] Y. Pennec, B. Djafari-Rouhani, J.O. Vasseur, A. Khelif, P.A. Deymier, Tunable filtering and demultiplexing in phononic crystals with hollow cylinders, Phys. Rev. E 69 (4) (2004) 046608.
[12] H. Zhu, F. Semperlotti, Metamaterial based embedded acoustic filters for structural applications, AIP Adv. 3 (9) (2013).
[13] N. Boechler, G. Theocharis, S. Job, P.G. Kevrekidis, M.A. Porter, C. Daraio, Discrete breathers in one-dimensional diatomic granular crystals, Phys. Rev. Lett. 104 (24) (2010) 244302.
[14] H. Shao, G. Chen, H. He, Elastic wave localization and energy harvesting defined by piezoelectric patches on phononic crystal waveguide, Phys. Lett. A 403 (2021) 127366.
[15] V.A. Lvov, F.S. Senatov, A.A. Veveris, V.A. Skrybykina, A. Díaz Lantada, Auxetic metamaterials for biomedical devices: current situation, main challenges, and research trends, Materials 15 (4) (2022) 1439.
[16] S. Raghavan, V. Rajeshkumar, An overview of metamaterials in biomedical applications, Prog. Electromagn. Res. 25 (2013) 369.
[17] K. Lu, J.H. Wu, D. Guan, N. Gao, L. Jing, A lightweight low-frequency sound insulation membrane-type acoustic metamaterial, Aip Adv. 6 (2) (2016).
[18] Y. Zhang, J. Zhang, Y. Li, D. Yao, Y. Zhao, Y. Ai, W. Pan, J. Li, Research progress on thin-walled sound insulation metamaterial structures, in: Acoustics, Vol. 6, MDPI, 2024, pp. 298–330.
[19] X. Hou, V.V. Silberschmidt, Metamaterials with negative poisson's ratio: A review of mechanical properties and deformation mechanisms, Mech. Adv. Mater.: Anal. Prop. Perform. (2015) 155–179.
[20] S. Babaee, J. Shim, J.C. Weaver, E.R. Chen, N. Patel, K. Bertoldi, 3D soft metamaterials with negative Poisson's ratio, Adv. Mater. 25 (36) (2013) 5044–5049.
[21] R. Graciá-Salgado, V.M. García-Chocano, D. Torrent, J. Sánchez-Dehesa, Negative mass density and ρ-near-zero quasi-two-dimensional metamaterials: Design and applications, Phys. Rev. B 88 (22) (2013) 224305.
[22] H. Huang, C. Sun, G. Huang, On the negative effective mass density in acoustic metamaterials, Internat. J. Engrg. Sci. 47 (4) (2009) 610–617.
[23] T. Klatt, M.R. Haberman, A nonlinear negative stiffness metamaterial unit cell and small-on-large multiscale material model, J. Appl. Phys. 114 (3) (2013).
[24] X. Tan, S. Chen, B. Wang, J. Tang, L. Wang, S. Zhu, K. Yao, P. Xu, Real-time tunable negative stiffness mechanical metamaterial, Extrem. Mech. Lett. 41 (2020) 100990.
[25] C. Luyun, H. Xichun, Acoustic cloaking design based on penetration manipulation with combination acoustic metamaterials, J. Low Freq. Noise Vib. Act. Control. 43 (1) (2024) 429–436.
[26] Q. Zhang, G. Hu, S. Rudykh, Magnetoactive asymmetric mechanical metamaterial for tunable elastic cloaking, Int. J. Solids Struct. 289 (2024) 112648.
[27] S. Yang, J.H. Page, Z. Liu, M.L. Cowan, C.T. Chan, P. Sheng, Focusing of sound in a 3D phononic crystal, Phys. Rev. Lett. 93 (2) (2004) 024301.
[28] S. Tol, F. Degertekin, A. Erturk, 3D-printed phononic crystal lens for elastic wave focusing and energy harvesting, Addit. Manuf. 29 (2019) 100780.
[29] J. Fan, L. Zhang, S. Wei, Z. Zhang, S.-K. Choi, B. Song, Y. Shi, A review of additive manufacturing of metamaterials and developing trends, Mater. Today 50 (2021) 303–328.
[30] Y. Sun, W. Ye, Y. Chen, W. Fan, J. Feng, P. Sareh, Geometric design classification of kirigami-inspired metastructures and metamaterials, in: Structures, Vol. 33, Elsevier, 2021, pp. 3633–3643.
[31] L. Shi, W. Xuan, B. Zhang, S. Dong, H. Jin, J. Luo, Numerical investigation of phononic crystal based film bulk acoustic wave resonators, Nanomaterials 11 (10) (2021) 2547.
[32] Y. Du, W. Wu, W. Chen, Y. Lin, Q. Chi, Control the structure to optimize the performance of sound absorption of acoustic metamaterial: A review, AIP Adv. 11 (6) (2021).
[33] C. Mercer, T. Speck, J. Lee, D.S. Balint, M. Thielen, Effects of geometry and boundary constraint on the stiffness and negative Poisson's ratio behaviour of auxetic metamaterials under quasi-static and impact loading, Int. J. Impact Eng. 169 (2022) 104315.
[34] M. Miniaci, A. Krushynska, A.B. Movchan, F. Bosia, N.M. Pugno, Spider web-inspired acoustic metamaterials, Appl. Phys. Lett. 109 (7) (2016).
[35] W. Kuang, Z. Hou, Y. Liu, The effects of shapes and symmetries of scatterers on the phononic band gap in 2D phononic crystals, Phys. Lett. A 332 (5–6) (2004) 481–490.
[36] A. Khelif, Y. Achaoui, S. Benchabane, V. Laude, B. Aoubiza, Locally resonant surface acoustic wave band gaps in a two-dimensional phononic crystal of pillars on a surface, Phys. Rev. B— Condens. Matter Mater. Phys. 81 (21) (2010) 214303.
[37] J.-J. Chen, S.-Y. Huo, Z.-G. Geng, H.-B. Huang, X.-F. Zhu, Topological valley transport of plate-mode waves in a homogenous thin plate with periodic stubbed surface, AIP Adv. 7 (11) (2017).
[38] Y. Bao, Z. Yao, X. Hu, X. Liu, Y. Shan, T. He, Complete bandgap of three-dimensional helical metamaterial tapered rod with power-law radius, Mech. Syst. Signal Process. 211 (2024) 111257.
[39] X. Zhou, Y. Xu, Y. Liu, L. Lv, F. Peng, L. Wang, Extending and lowering band gaps by multilayered locally resonant phononic crystals, Appl. Acoust. 133 (2018) 97–106.
[40] G. Anatriello, G. Vincenzi, Logarithmic spirals and continue triangles, J. Comput. Appl. Math. 296 (2016) 127–137.
[41] K. Tsuji, S.C. Müller, Spirals and Vortices, Springer, 2019.
[42] T.A. Cook, The Curves of Life: Being an Account of Spiral Formations and Their Application to Growth in Nature, to Science, and to Art: with Special Reference to the Manuscripts of Leonardo Da Vinci, Courier Corporation, 1979.
[43] T. Heath, The Works of Archimedes, Dover, 2002.
[44] M. Jafarpour, S. Gorb, H. Rajabi, Double-spiral: a bioinspired pre-programmable compliant joint with multiple degrees of freedom, J. R. Soc. Interface 20 (198) (2023) 20220757.
[45] S. Zhang, J. Hui Wu, Z. Hu, Low-frequency locally resonant band-gaps in phononic crystal plates with periodic spiral resonators, J. Appl. Phys. 113 (16) (2013).
[46] H. Gao, Q. Yan, X. Liu, Y. Zhang, Y. Sun, Q. Ding, L. Wang, J. Xu, H. Yan, Low-frequency bandgaps of the lightweight single-phase acoustic metamaterials with locally resonant archimedean spirals, Materials 15 (1) (2022) 373.
[47] S. Li, J. Yang, Topological transition in spiral elastic valley metamaterials, Phys. Rev. Appl. 15 (1) (2021) 014058.
[48] M.H. Bae, W. Choi, J.M. Ha, M. Kim, H.M. Seung, Extremely low frequency wave localization via elastic foundation induced metamaterial with a spiral cavity, Sci. Rep. 12 (1) (2022) 3993.
[49] M. Kheybari, Z. Wang, H. Xu, O.R. Bilal, Programmability of ultrathin metasurfaces through curvature, Extrem. Mech. Lett. 52 (2022) 101620.
[50] M. Kheybari, O.R. Bilal, Harnessing asymmetry to reprogram nonlinear metamaterials on-the-fly with no moving parts, Mater. Des. 233 (2023) 112168.
[51] Y. Ruan, X. Liang, X. Hua, C. Zhang, H. Xia, C. Li, Isolating low-frequency vibration from power systems on a ship using spiral phononic crystals, Ocean Eng. 225 (2021) 108804.
[52] A. Foehr, O.R. Bilal, S.D. Huber, C. Daraio, Spiral-based phononic plates: From wave beaming to topological insulators, Phys. Rev. Lett. 120 (20) (2018) 205501.
[53] H. Zhai, H. Xiang, X. Ma, J. Xiang, Optimal bandgaps of a spiral structure based on locally resonant phononic crystals, Internat. J. Modern Phys. B 33 (22) (2019) 1950256.
[54] H. Xiang, X. Ma, J. Xiang, Optimization for a locally resonant phononic crystal of square spiral with circle inside, IEEE Access 7 (2019) 145988–145995.
[55] Z. Chai, T. Zheng, J. Xiang, Design a low-frequency vibration energy harvesting device based on a square spiral beam local resonant phononic crystal, Phys. B 679 (2024) 415792.
[56] J.-S. Chen, T.-Y. Chen, Y.-C. Chang, Metastructures with double-spiral resonators for low-frequency flexural wave attenuation, J. Appl. Phys. 130 (1) (2021).
[57] H. Liu, Z. Shi, Y. Wang, H. Zhai, A band gap optimization scheme for two-dimensional locally resonant phononic crystal with square spiral rings, Phys. Lett. A 442 (2022) 128134.
[58] Y. Du, M.A. Akbar, Z. Zhang, T. Kalaida, Q.-H. Qin, Spiral rod–mass 3D phononic metamaterial with tunable low and ultra-wide bandgap, Int. J. Appl. Mech. 17 (2) (2025) 2550009.
[59] Z. Guo, Z. Li, K. Zeng, J. Ye, X. Lu, Z. Lei, Z. Wang, Fibonacci-array inspired modular acoustic metamaterials for tunable low-frequency absorption, Adv. Mater. Technol. 10 (2) (2025) 2400934.
[60] Z. Lu, H. Chen, L. Yao, Investigation of unidirectional vibration isolation and nonreciprocal design of axial elastic waves based on topological pumping theory, Int. J. Solids Struct. 309 (2025) 113192.
[61] E. Miranda Jr., E. Nobrega, S. Rodrigues, C. Aranas Jr., J. Dos Santos, Wave attenuation in elastic metamaterial thick plates: Analytical, numerical and experimental investigations, Int. J. Solids Struct. 204 (2020) 138–152.
[62] Y. Wang, F. Li, Y. Wang, K. Kishimoto, W. Huang, Tuning of band gaps for a two-dimensional piezoelectric phononic crystal with a rectangular lattice, Acta Mech. Sin. 25 (1) (2009) 65–71.
[63] V.F. Dal Poggetto, A.L. Serpa, Elastic wave band gaps in a three-dimensional periodic metamaterial using the plane wave expansion method, Int. J. Mech. Sci. 184 (2020) 105841.

[64] Y. Tanaka, Y. Tomoyasu, S.-i. Tamura, Band structure of acoustic waves in phononic lattices: Two-dimensional composites with large acoustic mismatch, Phys. Rev. B 62 (11) (2000) 7387.
[65] K. ElMahgoub, F. Yang, A. Elsherbeni, Scattering Analysis of Periodic Structures Using Finite-Difference Time-Domain Method, Springer Nature, 2022.
[66] M. Sigalas, N. Garcıa, Theoretical study of three dimensional elastic band gaps with the finite-difference time-domain method, J. Appl. Phys. 87 (6) (2000) 3122–3125.
[67] G. Wang, J. Wen, X. Wen, Quasi-one-dimensional phononic crystals studied using the improved lumped-mass method: Application to locally resonant beams with flexural wave band gap, Phys. Rev. B— Condens. Matter Mater. Phys. 71 (10) (2005) 104302.
[68] C. Yuan, L. Jing, Z. Jingdong, H. Tao, Z. Minggang, Y.D. Yuan, Phononic first band gap of quaternary layered periodic structure with the lumped-mass method, Shock. Vib. 2014 (1) (2014) 189539.
[69] X. Wang, L. Zhao, H. Liu, H. Shu, C. Lyu, W. Liu, X. Wang, X. Shi, Research on the design of phononic crystal rod band gaps based on lumped mass method, Mech. Solids 58 (2) (2023) 586–601.
[70] Q. Wei, J. Xiang, W. Zhu, H. Hu, Band structures analysis of fluid–solid phononic crystals using wavelet-based boundary element method and frequency-independent fundamental solutions, Internat. J. Numer. Methods Engrg. 124 (20) (2023) 4603–4633.
[71] Q. Wei, X. Ma, J. Xiang, Wavelet-based boundary element method for calculating the band structures of two-dimensional phononic crystals, Acta Mech. Solida Sin. 34 (2021) 687–705.
[72] Z.-Z. Yan, Y.-S. Wang, Wavelet-based method for calculating elastic band gaps of two-dimensional phononic crystals, Phys. Rev. B— Condens. Matter Mater. Phys. 74 (22) (2006) 224303.
[73] S. Xu, C. Qiu, Z. Liu, Acoustic transmission through asymmetric grating structures made of cylinders, J. Appl. Phys. 111 (9) (2012).
[74] J. Mei, Z. Liu, C. Qiu, Multiple-scattering theory for out-of-plane propagation of elastic waves in two-dimensional phononic crystals, J. Phys.: Condens. Matter. 17 (25) (2005) 3735.
[75] L. Cai, H. Xiaoyun, W. Xisen, Band-structure results for elastic waves interpreted with multiple-scattering theory, Phys. Rev. B— Condens. Matter Mater. Phys. 74 (15) (2006) 153101.
[76] W. Li, X. Kong, Q. Xu, Z. Hao, Bandgap accuracy and characteristics of fluid-filled periodic pipelines utilizing precise parameters transfer matrix method, J. Fluids Struct. 127 (2024) 104136.
[77] H.-S. Shu, X.-G. Wang, R. Liu, X.-G. Li, X.-N. Shi, S.-J. Liang, L.-H. Xu, F.-Z. Dong, Bandgap analysis of cylindrical shells of generalized phononic crystals by transfer matrix method, Internat. J. Modern Phys. B 29 (24) (2015) 1550176.
[78] Z.-Q. Ni, Y. Zhang, L.-H. Jiang, L. Han, Bending vibration band structure of phononic crystal beam by modified transfer matrix method, Internat. J. Modern Phys. B 28 (15) (2014) 1450093.
[79] W. Guo, X. Hong, W. Luo, J. Yan, J. Deng, J. Yang, New bandgap analysis method for metamaterial structures using variational principle, Eur. J. Mech. A Solids 106 (2024) 105344.
[80] T. Wang, M.-P. Sheng, Q.-H. Qin, Multi-flexural band gaps in an Euler–Bernoulli beam with lateral local resonators, Phys. Lett. A 380 (4) (2016) 525–529.
[81] W. Guo, Z. Yang, Q. Feng, C. Dai, J. Yang, X. Lei, A new method for band gap analysis of periodic structures using virtual spring model and energy functional variational principle, Mech. Syst. Signal Process. 168 (2022) 108634.
[82] K.H. Matlack, M. Serra-Garcia, A. Palermo, S.D. Huber, C. Daraio, Designing perturbative metamaterials from discrete models, Nat. Mater. 17 (4) (2018) 323–328.
[83] M.I. Hussein, Reduced Bloch mode expansion for periodic media band structure calculations, Proc. R. Soc. A: Math. Phys. Eng. Sci. 465 (2109) (2009) 2825–2848.
[84] D. Krattiger, M.I. Hussein, Generalized Bloch mode synthesis for accelerated calculation of elastic band structures, J. Comput. Phys. 357 (2018) 183–205.
[85] S. Ebrahimi-Nejad, M. Kheybari, Composite locally resonating stop band acoustic metamaterials, Acta Acust. United Acust. 105 (2) (2019) 313–325.
[86] S. Ebrahimi-Nejad, M. Kheybari, Honeycomb locally resonant absorbing acoustic metamaterials with stop band behavior, Mater. Res. Express 5 (10) (2018) 105801.
[87] M. Kheybari, C. Daraio, O.R. Bilal, Tunable auxetic metamaterials for simultaneous attenuation of airborne sound and elastic vibrations in all directions, Appl. Phys. Lett. 121 (8) (2022).
[88] Y. Liu, L.-t. Gao, Explicit dynamic finite element method for band-structure calculations of 2D phononic crystals, Solid State Commun. 144 (3–4) (2007) 89–93.
[89] I.A. Veres, T. Berer, O. Matsuda, Complex band structures of two dimensional phononic crystals: Analysis by the finite element method, J. Appl. Phys. 114 (8) (2013).
[90] E.B. Chin, A.A. Mokhtari, A. Srivastava, N. Sukumar, Spectral extended finite element method for band structure calculations in phononic crystals, J. Comput. Phys. 427 (2021) 110066.
[91] S. Liu, P.-p. Liu, R.-j. Zhao, J.-h. Lu, K. Yang, H. Zhou, Y.-f. Du, Study on acoustic performance of new spiral sound absorbing and insulating metamaterial, J. Low Freq. Noise Vib. Act. Control. 43 (2) (2024) 939–955.
[92] Y. Kusano, J. Segovia-Fernandez, S. Sonmezoglu, R. Amirtharajah, D.A. Horsley, Frequency selective MEMS microphone based on a bioinspired spiral-shaped acoustic resonator, in: 2017 19th International Conference on Solid-State Sensors, Actuators and Microsystems, TRANSDUCERS, IEEE, 2017, pp. 71–74.
[93] M. Kheybari, S. Ebrahimi-Nejad, Dual-target-frequency-range stop-band acoustic metamaterial muffler: acoustic and CFD approach, Eng. Res. Express 3 (3) (2021) 035027.
[94] M. Kheybari, S. Ebrahimi-Nejad, Locally resonant stop band acoustic metamaterial muffler with tuned resonance frequency range, Mater. Res. Express 6 (2) (2018) 025802.
[95] W. Li, F. Meng, Y. Chen, Y.f. Li, X. Huang, Topology optimization of photonic and phononic crystals and metamaterials: a review, Adv. Theory Simul. 2 (7) (2019) 1900017.
[96] H.-W. Dong, X.-X. Su, Y.-S. Wang, C. Zhang, Topological optimization of two-dimensional phononic crystals based on the finite element method and genetic algorithm, Struct. Multidiscip. Optim. 50 (4) (2014) 593–604.
[97] V.F. Dal Poggetto, F. Bosia, M. Miniaci, N.M. Pugno, Optimization of spider web-inspired phononic crystals to achieve tailored dispersion for diverse objectives, Mater. Des. 209 (2021) 109980.
[98] P. Kudela, A. Ijjeh, M. Radzienski, M. Miniaci, N. Pugno, W. Ostachowicz, Deep learning aided topology optimization of phononic crystals, Mech. Syst. Signal Process. 200 (2023) 110636.
[99] Z. Feng, W. Lei, L. Xu, S. Chen, H. Xu, Automated de novo design of architectured materials: Leveraging explainable artificial intelligence (XAI) for inspiration from stochastic microstructure outliers, Extrem. Mech. Lett. 73 (2024) 102269.
[100] M. Zhang, Q. Wang, Z. Luo, W. Gao, Stochastic bandgap optimization for multiscale elastic metamaterials with manufacturing imperfections, Int. J. Mech. Sci. 268 (2024) 109035.
[101] S. Rodriguez, E. Calius, A. Khatibi, A. Orifici, R. Das, An automated design framework for composite mechanical metamaterials and its application to 2D pentamode materials, Int. J. Mech. Sci. 276 (2024) 109393.
[102] T. Xue, S. Adriaenssens, S. Mao, Learning the nonlinear dynamics of mechanical metamaterials with graph networks, Int. J. Mech. Sci. 238 (2023) 107835.
[103] D. Lee, B.D. Youn, S.-H. Jo, Deep-learning-based framework for inverse design of a defective phononic crystal for narrowband filtering, Int. J. Mech. Sci. 255 (2023) 108474.
[104] S. Dedoncker, C. Donner, L. Taenzer, B. Van Damme, Generative inverse design of multimodal resonant structures for locally resonant metamaterials, 2023, arXiv preprint arXiv:2309.04177.
[105] D. Kreuzberger, N. Kühl, S. Hirschl, Machine learning operations (mlops): Overview, definition, and architecture, IEEE Access 11 (2023) 31866–31879.
[106] K. Naghavi Khanghah, Z. Wang, H. Xu, Reconstruction and generation of porous metamaterial units via variational graph autoencoder and large language model, J. Comput. Inf. Sci. Eng. (2024) 1–26.
[107] C.-X. Liu, G.-L. Yu, Z. Liu, Machine learning models in phononic metamaterials, Curr. Opin. Solid State Mater. Sci. 28 (2024) 101133.
[108] J. Ma, Phonon engineering of micro-and nanophononic crystals and acoustic metamaterials: A review, Small Sci. 3 (1) (2023) 2200052.
[109] G. Yu, L. Xiao, W. Song, Deep learning-based heterogeneous strategy for customizing responses of lattice structures, Int. J. Mech. Sci. 229 (2022) 107531.
[110] Z. Wang, W. Xian, M.R. Baccouche, H. Lanzerath, Y. Li, H. Xu, Design of phononic bandgap metamaterials based on Gaussian mixture beta variational autoencoder and iterative model updating, J. Mech. Des. 144 (4) (2022) 041705.
[111] W. Demeke, J. Jung, H. Song, B. Ryu, W. Jeon, S. Ryu, Design of aluminum plate phononic crystals with wide bandgaps via free-form shape optimization using deep neural networks, Extrem. Mech. Lett. 65 (2023) 102098.
[112] S.M. Sadat, R.Y. Wang, A machine learning based approach for phononic crystal property discovery, J. Appl. Phys. 128 (2) (2020).
[113] X. Li, S. Ning, Z. Liu, Z. Yan, C. Luo, Z. Zhuang, Designing phononic crystal with anticipated band gap through a deep learning based data-driven method, Comput. Methods Appl. Mech. Engrg. 361 (2020) 112737.
[114] Z. Wang, W. Xian, Y. Li, H. Xu, Embedding physical knowledge in deep neural networks for predicting the phonon dispersion curves of cellular metamaterials, Comput. Mech. 72 (1) (2023) 221–239.
[115] Y. Xu, H. Weng, X. Ju, H. Ruan, J. Chen, C. Nan, J. Guo, L. Liang, A method for predicting mechanical properties of composite microstructure with reduced dataset based on transfer learning, Compos. Struct. 275 (2021) 114444.
[116] Z. Wang, R. Zhuang, W. Xian, J. Tian, Y. Li, S. Chen, H. Xu, Phononic metamaterial design via transfer learning-based topology optimization framework, in: International Design Engineering Technical Conferences and Computers and Information in Engineering Conference, Vol. 86229, American Society of Mechanical Engineers, 2022, V03AT03A048.
[117] J.L. Deutsch, C.V. Deutsch, Latin hypercube sampling with multidimensional uniformity, J. Statist. Plann. Inference 142 (3) (2012) 763–772.
[118] P.A. Deymier, Acoustic Metamaterials and Phononic Crystals, Vol. 173, Springer Science & Business Media, 2013.

[119] X. Liang, J. Du, Design of phononic-like structures and band gap tuning by concurrent two-scale topology optimization, Struct. Multidiscip. Optim. 61 (3) (2020) 943–962.
[120] L. D'Alessandro, B. Bahr, L. Daniel, D. Weinstein, R. Ardito, Shape optimization of solid–air porous phononic crystal slabs with widest full 3D bandgap for in-plane acoustic waves, J. Comput. Phys. 344 (2017) 465–484.
[121] A. Dalklint, M. Wallin, K. Bertoldi, D. Tortorelli, Tunable phononic bandgap materials designed via topology optimization, J. Mech. Phys. Solids 163 (2022) 104849.
[122] C. Xiao, J. Ye, R.M. Esteves, C. Rong, Using spearman's correlation coefficients for exploratory data analysis on big dataset, Concurr. Comput.: Pr. Exp. 28 (14) (2016) 3866–3878.
[123] S. Javadi, A. Maghami, S.M. Hosseini, A deep learning approach based on a data-driven tool for classification and prediction of thermoelastic wave's band structures for phononic crystals, Mech. Adv. Mater. Struct. 29 (27) (2022) 6612–6625.